

Detection and manipulation of nuclear spin states in fermionic strontium

Simon Stellmer,^{1,2} Rudolf Grimm,^{1,2} and Florian Schreck¹

¹*Institut für Quantenoptik und Quanteninformation (IQOQI),
Österreichische Akademie der Wissenschaften, 6020 Innsbruck, Austria*

²*Institut für Experimentalphysik und Zentrum für Quantenphysik, Universität Innsbruck, 6020 Innsbruck, Austria*
(Dated: October 18, 2018)

Fermionic ^{87}Sr has a nuclear spin of $I = 9/2$, higher than any other element with similar electronic structure. This large nuclear spin has many applications in quantum simulation and computation, for which preparation and detection of the spin state are requirements. For an ultracold ^{87}Sr cloud, we show two complementary methods to characterize the spin-state mixture: optical Stern-Gerlach state separation and state-selective absorption imaging. We use these methods to optimize the preparation of a variety of spin-state mixtures by optical pumping and to measure an upper bound of the ^{87}Sr spin relaxation rate.

PACS numbers: 67.85.-d, 03.75.Ss, 37.10.Vz

I. INTRODUCTION

Fermions with two valence electrons, like ^{43}Ca , ^{87}Sr , ^{171}Yb , and ^{173}Yb , have a rich internal state structure, which is at the heart of recent proposals for quantum simulation and computation [1–14]. Unlike bosonic isotopes of these elements, the fermions have a nuclear spin, which decouples from the electronic degrees of freedom in the 1S_0 ground state and the 3P_0 metastable state. This gives rise to a $SU(N)$ spin symmetry, where N is the number of nuclear spin states, which can be as high as 10 for ^{87}Sr [1, 2]. Rich quantum phases have been predicted to exist in such Fermi systems [1–8]. The nuclear spin is also essential for the implementation of artificial non-abelian gauge fields [9, 11, 12]. Furthermore it can be used to robustly store quantum information, which can be manipulated using the electronic structure [13, 14]. After the recent attainment of quantum degeneracy in $^{171,173}\text{Yb}$ [15, 16] and ^{87}Sr [17, 18], these ideas are coming closer to realization.

Essential tools for quantum simulation and computation with these degenerate gases are the detection and manipulation of the spin-state mixture. Several alkaline-earth spin-state detection schemes were already demonstrated. The number of atoms in the highest m_F state was determined by selectively cooling [19] or levitating [18] atoms in this state. The number of atoms in an arbitrary m_F state was determined using state-selective shelving of atoms in a metastable state, which requires a “clock”-transition laser [20]. Recording the full m_F -state distribution with this method is possible, but needs one experimental run per state. Determination of the m_F -state distribution in only two experimental runs was recently shown for quantum-degenerate Yb gases, using optical Stern-Gerlach (OSG) separation [16].

In this Article, we first show two nuclear spin-state detection schemes for ^{87}Sr that have advantages over the previously used schemes. In Sec. II, we present an adaptation and extension of the OSG separation scheme of [16], which in our implementation is able to resolve all ten nuclear spin-states of Sr in a single experimental run. In Sec. III, we describe state-selective absorption imag-

ing using the intercombination line of Sr. Unlike OSG separation, this method gives spatial information about the spin-state distribution and is also applicable to samples before evaporative cooling. In Sec. IV, we demonstrate the preparation of a desired spin-state mixture by optical pumping, using spin-state detection to optimize the optical pumping procedure. In Sec. V, we determine an upper limit of the ^{87}Sr spin-relaxation rate, using our spin-state preparation and detection methods.

II. OPTICAL STERN-GERLACH SEPARATION

Here, we describe the operation principle of optical Stern-Gerlach (OSG) separation (Sec. IIA) and our experimental implementation (Sec. IIB). In Sec. IIC, we describe a simulation of the OSG process. In Sec. IID we determine the number of atoms in each spin state.

A. Operation principle

The Stern-Gerlach technique separates atoms in different internal states by applying a state-dependent force and letting the atomic density distribution evolve under this force [21]. The implementation of this technique for alkali atoms is simple. Their single valence electron provides them with a m_F -state dependent magnetic moment that, for easily achievable magnetic field gradients, results in m_F -state dependent forces sufficient for state separation [22]. By contrast, atoms with two valence electrons possess only a weak, nuclear magnetic moment in the electronic ground state, which would require the application of impractically steep magnetic field gradients. An alternative is OSG separation, where a state dependent dipole force is used. OSG separation was first shown for a beam of metastable helium [23], where orthogonal dressed states of the atoms were separated by a resonant laser field gradient. The case of interest here, OSG m_F -state separation, was recently realized for a quantum degenerate gas of Yb, by using m_F -state dependent dipole forces [16].

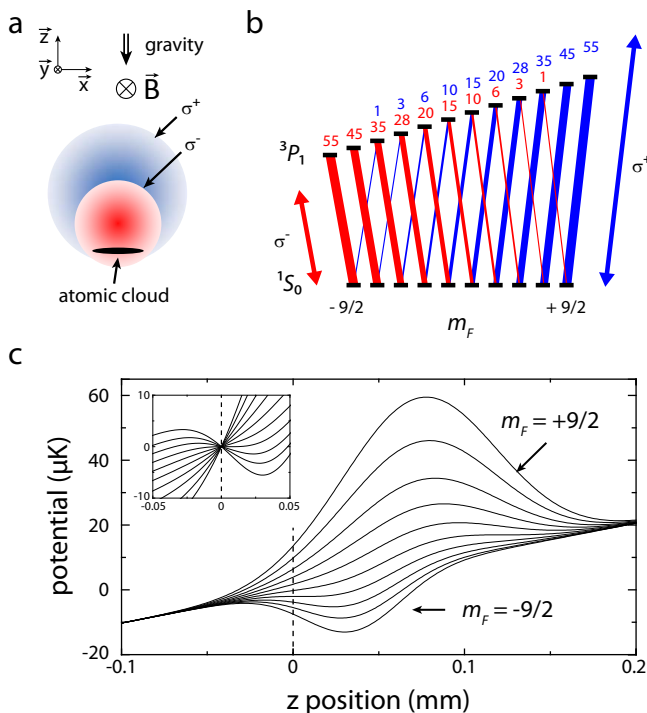


Figure 1: (Color online) Principle of OSG separation. a) σ^+ - and σ^- -polarized laser beams propagating in the y -direction create dipole forces on an atomic cloud that is located on the slopes of the Gaussian beams. b) The laser beams are tuned close to the $^1S_0(F = 9/2) - ^3P_1(F' = 11/2)$ intercombination line, creating attractive (σ^- beam) or repulsive (σ^+ beam) dipole potentials. Each m_F state experiences a different potential because of the varying line strength of the respective transition. c) The potentials resulting from dipole potentials and the gravitational potential. The dashed line marks the initial position of the atoms. The inset shows the relevant region of the potentials, offset shifted to coincide at the position of the atoms, which clearly shows the different gradient on each m_F state.

We first explain the basic operation principle of Sr OSG separation before discussing our experimental implementation. The experimental situation is shown in Fig. 1(a). An ultracold cloud of ^{87}Sr atoms in a mixture of m_F states is released from an optical dipole trap. The m_F -state dependent force is the dipole force of two laser beams propagating in the plane of the pancake-shaped cloud, one polarized σ^+ , the other σ^- . The diameter of these OSG laser beams is on the order of the diameter of the cloud in the x -direction. The beams are displaced vertically by about half a beam radius to produce a force in the z -direction on the atoms. To create a m_F -state dependent force, the OSG beams are tuned close to the $^1S_0(F = 9/2) - ^3P_1(F' = 11/2)$ intercombination line (wavelength 689 nm, linewidth 7.6 kHz), so that this line gives the dominant contribution to the dipole force. A guiding magnetic field is applied in the direction of the laser beams such that the beams couple only to σ^+ or σ^- transitions, respectively. The line strength of these transitions varies greatly with the m_F state [24],

see Fig. 1(b), resulting in different forces on the states. For ^{173}Yb , this variation, together with a beneficial summation of dipole forces from transitions to different 3P_1 hyperfine states, was sufficient to separate four of the six m_F states using just one OSG beam [16]. The remaining two m_F states could be analyzed by repeating the experiment with opposite circular polarization of the OSG beam.

Strontium, which has nearly twice as many nuclear spin states, requires an improved OSG technique to separate the states. The improvement consists of applying two OSG beams with opposite circular polarization at the same time. The σ^+ -polarized beam produces dipole forces mainly on the positive m_F states, the σ^- beam mainly on the negative m_F states. By positioning the beams in the appropriate way (see below), the forces point in opposite directions and all m_F states can be separated in a single experimental run. A second improvement is to enhance the difference in the dipole forces on neighboring m_F states by tuning already strong transitions closer to the OSG beam frequency using a magnetic field, which splits the excited state $m_{F'}$ states in energy. For our settings, the difference in forces on neighboring high $|m_F|$ states is enhanced by up to 25%, which helps to separate those states. This enhancement scheme requires the σ^+ -polarized OSG beam to be tuned to the blue of the resonance, whereas the σ^- beam has to be tuned to the red of the resonance, see Fig. 1(b). Both beams are centered above the atomic cloud so that the repulsive blue detuned beam produces a force pointing downwards, whereas the attractive red detuned beam produces a force pointing upwards.

B. Experimental demonstration

We demonstrate OSG separation of a cloud of 4.5×10^4 ^{87}Sr atoms in a mixture of m_F states. To prepare the cloud, Zeeman slowed ^{87}Sr atoms are laser cooled in two stages, first in a “blue” magneto-optical trap (MOT) on the broad-linewidth $^1S_0 - ^1P_1$ transition, then in a “red” MOT on the narrow-linewidth $^1S_0 - ^3P_1$ transition [17, 18]. Next, the atoms are transferred to a pancake-shaped optical dipole trap with strong confinement in the vertical direction. The sample is evaporatively cooled over seven seconds. At the end of evaporation the trap oscillation frequencies are $f_x = 19$ Hz, $f_y = 11$ Hz, and $f_z = 85$ Hz, where the coordinate system is defined in Fig. 1(a). The collision rate at this stage is only 1 s^{-1} , which is insufficient for complete thermalization. Since atoms are evaporated mainly downwards, along the z -direction, the sample is not in cross-dimensional thermal equilibrium, having a temperature of 25 nK in the z -direction and twice that value in the xy -plane. The sample is non-degenerate and the $1/e$ -widths of the Gaussian density distribution are $w_x = 55 \mu\text{m}$, $w_y = 85 \mu\text{m}$, and $w_z = 7 \mu\text{m}$.

The OSG beams propagate along the y -direction. The power of the σ^+ (σ^-) beam is 4 mW (0.5 mW), the waist

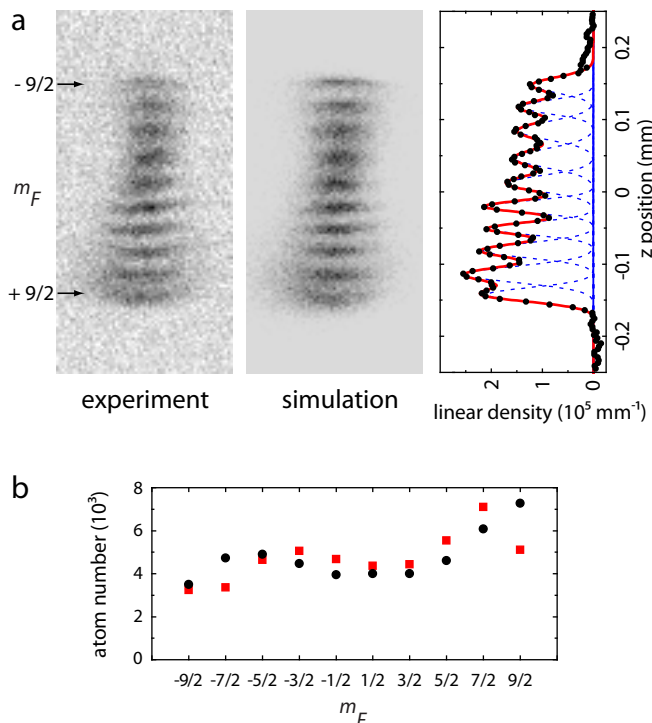


Figure 2: (Color online) OSG separation of the ten ^{87}Sr nuclear spin states. a) Atomic density distribution after OSG separation integrated over the $(\hat{x} + \hat{y})$ -direction obtained in experiment and simulation. On the right, the density distribution of the experiment integrated along the x - and y -directions is shown together with a fit consisting of ten Gaussian distributions. b) Atom number distribution determined from the area of the Gaussian distributions (squares) and the fit of the simulation to the experiment (circles).

is $\sim 80 \mu\text{m}$ ($\sim 60 \mu\text{m}$), and the beam center is displaced $\sim 70 \mu\text{m}$ ($\sim 40 \mu\text{m}$) above the cloud. Both beams create dipole forces of similar magnitude since the reduced power of the σ^- beam compared to the σ^+ beam is partially compensated by its decreased waist. At zero magnetic field, the σ^\pm beam is detuned ± 100 MHz from resonance. To increase the difference in dipole potential on neighboring m_F states, a magnetic field of 16 G is applied parallel to the OSG beams, which splits neighboring $^3P_1(F' = 11/2)$ $m_{F'}$ states by 6.1 MHz. With this field applied, the σ^\pm beam has a detuning of ± 66.4 MHz to the $^1S_0(F = 9/2, m_F = \pm 9/2) - ^3P_1(F' = 11/2, m_F = \pm 11/2)$ transition and a detuning of ± 133.6 MHz to the $^1S_0(F = 9/2, m_F = \mp 9/2) - ^3P_1(F' = 11/2, m_F = \mp 7/2)$ transition, see Fig. 1(b).

OSG separation is started by simultaneously releasing the atoms from the dipole trap and switching on the OSG beams. The atoms are accelerated for 1.6 ms by the OSG beams. Then the beams are switched off to avoid oscillations of atoms in the dipole trap formed by the red detuned OSG beam. The atoms freely expand for another 2.3 ms before an absorption image on the $^1S_0 - ^1P_1$ transition is taken. The result is shown in Fig. 2(a). All ten m_F states are clearly distinguishable from each other.

To obtain a good separation of the m_F states and an even spacing between them, OSG beam waists, the timing of the OSG separation sequence, the applied magnetic field, and the beam positions were optimized. We found that for all other parameters fixed, the position of the OSG beams is critical and has to be aligned to better than $10 \mu\text{m}$.

To quantify the separation of the states, we fit ten Gaussian distributions to the density distribution integrated along the x - and y -directions, see Fig. 2(a). We obtain a separation of adjacent states between 28 and $38 \mu\text{m}$, similar to the $1/e$ -widths of the distributions, which are between 24 and $36 \mu\text{m}$. The $1/e$ -width expected from initial size and temperature after 3.9 ms total expansion time is $19 \mu\text{m}$ in the z -direction, slightly narrower than the width of the narrowest distributions observed. From the Gaussian fits we also obtain an estimation of the atom number in each state, see Sec. IID.

OSG separation works only well for very cold samples. If the temperature is too high, the sample expands too fast and the individual m_F -state distributions cannot be distinguished. For a density minimum to exist between two neighboring m_F -state distributions of Gaussian shape, the $1/e$ -widths have to be smaller than $\sqrt{2}$ times the distance between the maxima of the distributions. For our smallest separation of $24 \mu\text{m}$, this condition corresponds to samples with a temperature below 100 nK, which can only be obtained by evaporative cooling.

C. Simulation

We perform a simulation of classical trajectories of atoms to better understand the OSG separation process. The simulation takes into account the dipole potentials of the OSG beams, discrete spontaneous scattering events of OSG beam photons, and gravity. The phase-space distribution of simulated atoms is initialized using the experimentally measured trap frequencies and temperatures. The calculated density distributions are fit to the experimental result using the OSG beam waists and positions and the atom number of each state as fit parameters. The detunings and intensities of the OSG beams and the value of the magnetic field are fixed to the values used in the experiment [25]. The parameters of the σ^+ (σ^-) beam resulting in the best fit are a waist of $90 \mu\text{m}$ ($56 \mu\text{m}$) and a displacement of the beam center relative to the atomic cloud's center by $74 \mu\text{m}$ ($35 \mu\text{m}$) in the z -direction and by $0 \mu\text{m}$ ($7 \mu\text{m}$) in the x -direction. With these parameters, the simulation matches the experimental result well, see Fig. 2(a).

We now analyze the OSG separation process in detail using the simulation. The OSG beam potential gradients on atoms in different m_F states are nearly evenly distributed between 47m/s^2 downwards for the $+9/2$ state and 32m/s^2 upwards for the $-9/2$ state (see inset of Fig. 1(c)), resulting in the nearly evenly spaced m_F -state distribution after OSG separation. About 25% of

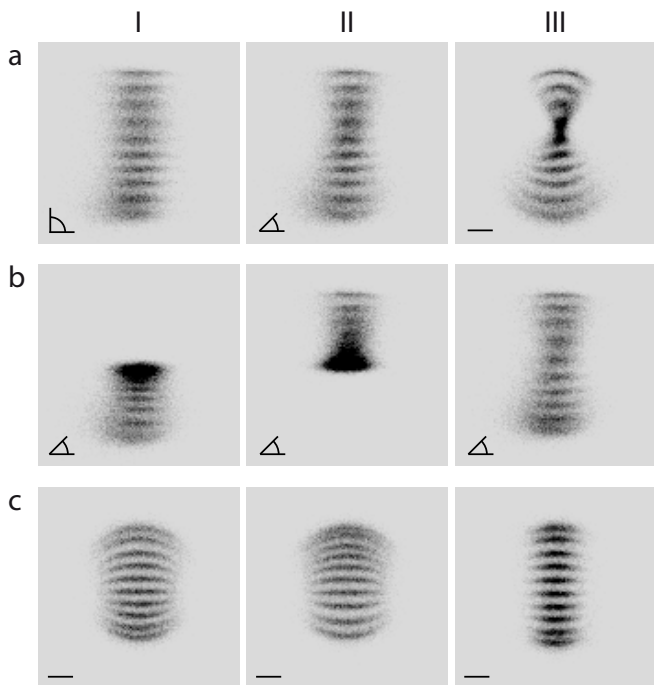


Figure 3: Simulated density distributions of atoms after OSG separation. Shown are distributions integrated along x (aI), along the $(\hat{x} + \hat{y})$ -direction (aII,b), and along y (aIII,c). The angle symbols indicate the angle between the direction of integration and the direction of the OSG beams, the y -direction. a) The density distribution obtained from a simulation with parameters fitted to the outcome of the experiment, integrated along different directions. The experimental situation corresponds to (aII). b) Influence of the two OSG beams and the magnetic field on OSG separation. bI) As (aII), but no σ^- beam. bII) As (aII), but no σ^+ beam. bIII) As (aII), but no magnetic field and reduced OSG beam detuning. c) Alternative scheme of OSG separation using two blue detuned OSG beams and variations of that scheme, see main text.

the atoms spontaneously scatter photons from the OSG beams, which leads to a widening of the individual m_F -state distributions in the z -direction by at most 20%, which only insignificantly reduces our ability to distinguish the m_F states.

Also the 3P_1 $F' = 7/2$ and $F' = 9/2$ hyperfine levels contribute noticeably to the dipole forces created by the OSG beams on the low $|m_F|$ states, which at first glance might be surprising since the detuning of the OSG beams from those states is more than an order of magnitude larger than the detuning from the $F' = 11/2$ state. The reason is that the dipole forces from the σ^+ and σ^- OSG beams considering only the $F' = 11/2$ hyperfine level nearly compensate each other for low $|m_F|$ states, whereas the dipole forces from both beams considering the other hyperfine levels point into the same direction and in addition are strongest for low $|m_F|$ states. The positions of the low $|m_F|$ states after a simulated OSG separation with and without considering the influence of the $F' = 7/2$ and $F' = 9/2$ levels changes by up to $13 \mu\text{m}$. By contrast, the positions of the $m_F = \pm 9/2$

states are changed by less than $2 \mu\text{m}$. It is not possible to obtain a good fit of the simulation to the experiment if the influence of the 3P_1 $F' = 7/2$ and $F' = 9/2$ hyperfine levels is neglected.

The shape of the density distribution is analyzed in row (a) of Fig. 3. The density distribution is shown as it would appear using absorption imaging along the x - (aI), the $(\hat{x} + \hat{y})$ - (aII), or the y -direction (aIII). Case (aII) is the one realized in the experiment. Strong distortions of the spatial distribution of each m_F state compared to a free expansion are visible. They are induced by the finite size of the OSG beams. The blue detuned beam expels high m_F -state atoms onto cylindrical surfaces, whereas the red detuned beam attracts low m_F -state atoms and acts like a focussing lens.

The role of each OSG beam and the magnetic field are demonstrated in row (b) of Fig. 3. Shown are the results of simulations with only the blue (bI) or the red (bII) detuned OSG beam present. With only one OSG beam, at best four m_F states can be well separated, illustrating the need of two beams for Sr OSG separation. In simulation (bIII) the magnetic field was set to zero, which removes the energy splitting of the $^3P_1(F' = 11/2)$ manifold. To achieve the same acceleration on the $m_F = \pm 9/2$ states as with magnetic field, the detuning of the σ^\pm OSG beam was set to ± 66.4 MHz from the center of the $F' = 11/2$ manifold. Without magnetic field, the spatial splitting between neighboring high $|m_F|$ states is slightly reduced. To separate these states further than done in the experiment, a larger magnetic field could be used.

The simulation also suggests an alternative OSG separation scheme, which is demonstrated in row (c) of Fig. 3, but which we did not check experimentally. Instead of one blue and one red detuned OSG beam, the scheme uses two blue detuned OSG beams of opposite circular polarization. As before, the σ^+ beam is placed above the cloud, acts mainly on the high m_F -state atoms and pushes them downwards. The σ^- beam uses now the same detuning, power, and waist as the σ^+ beam, but is placed below the initial center of the atomic cloud. The location of the two beams in the z -direction is symmetric with respect to the initial position of the atomic cloud. The σ^- beam acts mainly on the negative m_F -state atoms and pushes them upwards. Since this beam is now blue detuned, it does not act similar to a lens as the red detuned σ^- beam used in the experiment and leads to less distortion of the cloud. Three cases of this alternative scheme are shown in row (c), always assuming an even atom number distribution over the m_F states. Case (cI) uses σ^+ -beam parameters equivalent to the ones used for the simulations of row (a) and σ^- -beam parameters deduced from those as described above. In addition the magnetic field is set to zero. This situation leads to a nearly symmetric separation of positive and negative m_F states, where the symmetry is only slightly broken by gravity. Compared to the situation realized in the experiment, atoms in low m_F states are better separated.

One slight drawback of this scheme is that the application of a magnetic field as used in the experiment will only increase separation of positive m_F states. The separation of negative m_F states will even be decreased. This effect is demonstrated in case (cII), where a magnetic field similar to the one used in the experiment is assumed and the detunings of the OSG beams changed such that the initial accelerations of the $m_F = \pm 9/2$ states are the same as in case (cI). The reason for the decreased separation of negative m_F states is a reduction of the difference in the dipole forces of the σ^- beam on neighboring m_F states. This reduction comes from the Zeeman splitting of the $^3P_1 F' = 11/2$ level, which will tune transitions with strong line strength farther away from the σ^- -beam wavelength than transitions with weak line strength.

The distortions of the density distribution after OSG separation can be reduced if more power is available for the OSG beams. Then the waist of the OSG beams can be made wider in the x -direction keeping the same potential in the z -direction. This leads to a reduction of unwanted potential gradients along x , which are the source of the distortions well visible e.g. in (aIII) or (cI). The reduction is demonstrated in case (cIII), where the power and waist in the x -direction of the OSG beams has been doubled compared to case (cI).

D. Determination of the atom number distribution

To obtain the number of atoms in each m_F state, we use two approaches. The first one determines the atom numbers from ten Gaussian fits to the density distribution integrated along the x - and y -directions, see Fig. 2(a). The second approach uses the fit of the simulation to the data described above, which takes the distortions of the distribution better into account, but relies on our ability to accurately model the OSG separation process. A systematic effect should be considered in both approaches: the m_F -state dependence of the average photon number absorbed by an atom during absorption imaging. This dependence has its origin in the m_F -state dependent line strength of the absorption imaging transition. Under our imaging conditions (probe beam of circularly polarized light on the 1S_0 - 1P_1 transition with an intensity of 0.5 mW/cm^2 , an angle of 45° to the quantization axis given by the magnetic field, and $40 \mu\text{s}$ exposure time) in average about 40 photons are scattered per atom, making optical pumping during absorption imaging important. We simulate this optical pumping process to obtain an estimate of the number of photons scattered by an atom in dependence of its initial m_F state. We find that the optical pumping process depends strongly on the detuning of the absorption imaging beam to the closely spaced hyperfine states of the 1P_1 excited state, which are mixed at the 16 G magnetic field applied. Because of this dependence, not only the absolute number of photons scattered per atom depends on the detuning, but also the ratio of the number of photons scattered for different initial states. For atoms starting

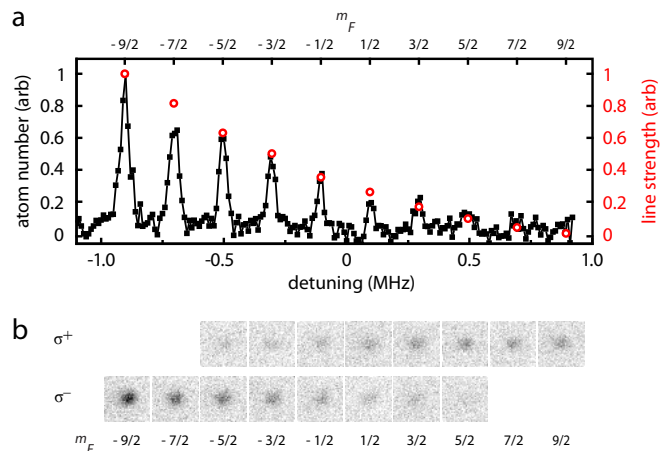


Figure 4: (Color online) m_F -state resolved absorption imaging on the $^1S_0(F = 9/2) - ^3P_1(F' = 11/2)$ intercombination line. a) Spectrum of a ^{87}Sr sample with nearly homogeneous m_F -state distribution. The spectrum was obtained using σ^- -polarized light and shifting transitions corresponding to different m_F states in frequency by applying a magnetic field of 0.5 G. The circles give the line strengths of the transitions. b) Absorption images taken on the maxima of absorption of each m_F state using σ^+ or σ^- polarized light.

in the $m_F = +9/2$ or the $m_F = -9/2$ state the ratio is highest, about 1.2(2), where the error comes from the uncertainty of the laser detuning used in the experiment. Further experimental study of this effect is needed to determine the relative atom numbers better. Simply assuming equal and maximal absorption by atoms in each m_F state, the atom number distributions resulting from the two approaches are shown in Fig. 2(b). The atom numbers of both approaches agree to better than 20% for all but two m_F states. The agreement is less good for the $m_F = +9/2$ state, which has the most distorted distribution, and the $m_F = -7/2$ state, for which the Gaussian fit underestimates the width.

III. SPIN-STATE DEPENDENT ABSORPTION IMAGING

We also demonstrate a complementary method of m_F -state detection: m_F -state dependent absorption imaging. This method is often used for alkali atoms employing a broad linewidth transition [26]. For Sr, m_F -state resolved imaging on the broad 1S_0 - 1P_1 transition is not possible since the magnetic field splitting of the excited state $m_{F'}$ states is smaller than the linewidth of the transition [20]. But m_F -state dependent imaging can be realized using the narrow $^1S_0(F = 9/2) - ^3P_1(F' = 11/2)$ intercombination line. To achieve state selectivity, we apply a magnetic field of 0.5 G, which splits neighboring $m_{F'}$ states by 200 kHz, which is 27 times more than the linewidth of the imaging transition. The advantages of this method compared to OSG separation is its applicability to samples that have not been evaporatively cooled, spatially resolved imaging, and a near perfect

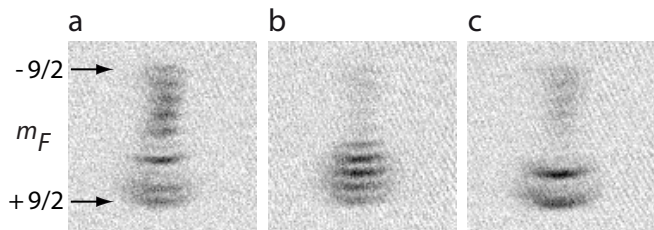


Figure 5: Examples of state mixtures prepared by optical pumping and analyzed using OSG separation. (a) The $m_F = 1/2$ and $5/2$ states were pumped to the $3/2$ state using σ^+ and σ^- light, respectively. (b) The negative m_F states were pumped to the positive m_F states. (c) A two-state mixture obtained by pumping the lower m_F states to the $m_F = 5/2$ and $7/2$ states and subsequently pumping the $m_F = 7/2$ state to the $m_F = 9/2$ state.

suppression of signal from undesired m_F states. A disadvantage of this method is that it delivers a reduced signal compared to imaging on the 1S_0 - 3P_1 transition, as done after OSG separation. The reduction comes from the narrower linewidth, optical pumping to dark states during imaging, and weak line strengths for some m_F states. Figure 4 shows a spectroscopy scan and absorption images taken on the maxima of the absorption signal for a sample with nearly homogeneous m_F -state distribution. The absorption is strongly m_F -state dependent and to obtain the best signal, the polarization of the absorption imaging light has to be adapted to the m_F state of interest: σ^+ (σ^-) for high (low) m_F states and π for low $|m_F|$ states. For our absorption imaging conditions (an intensity of $15 \mu\text{W}/\text{cm}^2$, which is 5 times the saturation intensity, and an exposure time of $40 \mu\text{s}$), even atoms in m_F states corresponding to the strongest transition will on average scatter less than one photon. Therefore the absorption is expected to be nearly proportional to the m_F -state dependent line strength of the transition, which we confirm using a simulation of the absorption imaging process [27].

IV. PREPARATION OF SPIN-STATE MIXTURES

For applications of ^{87}Sr to quantum simulation and computation, the m_F -state mixture needs to be controlled. We produce a variety of different mixtures by optical pumping, making use of OSG separation to quickly optimize the optical pumping scheme and quantify the result. Optical pumping is performed on the $^1S_0(F = 9/2) - ^3P_1(F' = 9/2)$ intercombination line, before evaporative cooling. A field of 3 G splits neighboring excited state $m_{F'}$ states by 255 kHz. This splitting is well beyond the linewidth of the transition of 7.4 kHz, allowing transfer of atoms from specific m_F states to neighboring states using σ^\pm - or π -polarized light, the choice depending on the desired state mixture. Sequences of pulses on different m_F states can create a wide variety of state mixtures, of which three examples are shown

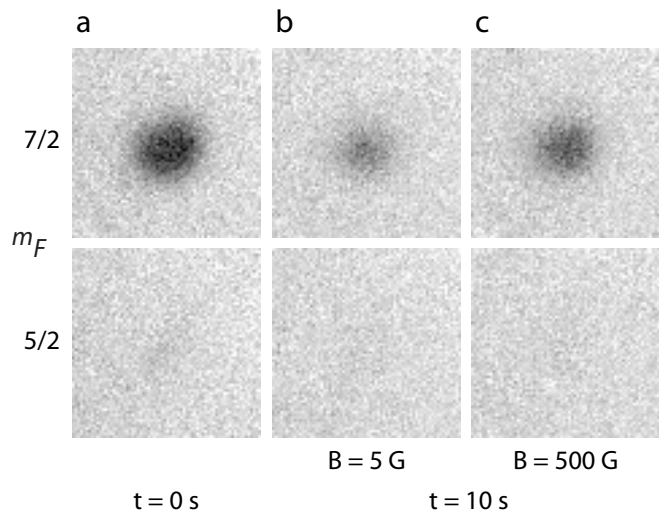


Figure 6: Absence of spin relaxation in ^{87}Sr . Shown are absorption images of the $m_F = 5/2$ and $7/2$ state averaged over 25 runs of the experiment. Atoms were initially removed from the $m_F = 5/2$ state by optical pumping, whereas all other m_F states remained populated (a). After 10 s hold at a magnetic field of 5 G (b) or 500 G (c) no $m_F = 5/2$ atoms are detectable, showing the low rate of spin relaxation.

in Fig. 5. Optical pumping on the $^1S_0(F = 9/2) - ^3P_1(F' = 7/2)$ and $^1S_0(F = 9/2) - ^3P_1(F' = 11/2)$ transitions yields similar results.

V. DETERMINATION OF AN UPPER BOUND OF THE SPIN-RELAXATION RATE

A low nuclear spin-relaxation rate is an essential requirement to use ^{87}Sr for quantum simulation and computation [1, 2]. The rate is expected to be small since the nuclear spin does not couple to the electronic degrees of freedom in the ground state. Here, we use our nuclear spin state preparation and detection techniques to determine an upper bound for this spin relaxation rate. We start with a sample of 1.5×10^6 atoms with near uniform m_F -state distribution and a temperature of $T = 1.5 \mu\text{K}$, confined in a trap with oscillation frequencies $f_x = 67 \text{ Hz}$, $f_y = 68 \text{ Hz}$, and $f_z = 360 \text{ Hz}$, obtained directly after transferring the atoms from the magneto-optical trap to the dipole trap without any further evaporation. We optically pump all atoms from the $m_F = 5/2$ state to neighboring states and look out for the reappearance of atoms in this state by spin relaxation during 10 s of hold. The atom number in the $m_F = 5/2$ state and, as a reference, the $m_F = 7/2$ state are determined from absorption images. During 10 s of hold at a magnetic field of either 5 G or 500 G the number of $m_F = 5/2$ atoms remains below our detection threshold of about 10^4 atoms, indicating a low spin-relaxation rate, see Fig. 6. From this observation, we can obtain an upper bound for the spin-relaxation rate. To obtain a conservative bound, we assume that the dominant process leading to the creation of $m_F = 5/2$ -state atoms

are collisions of $m_F = 7/2$ - with $m_F = 3/2$ -state atoms, forming two $m_F = 5/2$ -state atoms. Since the second order Zeeman effect is negligible no energy is released in such a collision and the resulting $m_F = 5/2$ -state atoms will remain trapped. The number of atoms created in the $m_F = 5/2$ state by spin relaxation after a hold time t is $N_{5/2} = 2N_{\text{state}}g_{\text{sr}}\bar{n}t$, where $N_{\text{state}} = 1.5 \times 10^5$ is the atom number in each populated state, g_{sr} the spin-relaxation rate constant, $\bar{n} = 7.5 \times 10^{11} \text{ cm}^{-3}$ the mean density and the factor 2 takes into account that two atoms are produced in the $m_F = 5/2$ state per collision. From our measurement we know that $N_{5/2} < 10^4$, from which we obtain an upper bound of $5 \times 10^{-15} \text{ cm}^3\text{s}^{-1}$ for the spin-relaxation rate constant. This bound for the rate constant corresponds for our sample to a spin relaxation rate which is 2000 times smaller than the elastic scattering rate. The rate constant could be even orders of magnitude smaller than the already low upper bound we obtained [28].

VI. CONCLUSION

In conclusion, we have demonstrated two complementary methods to characterize the spin-state mixture of

an ultracold cloud of ^{87}Sr . Optical Stern-Gerlach separation can characterize the spin-state mixture of an evaporatively cooled sample in a single experimental run and is very useful for fast optimization of optical pumping, which we have demonstrated by three examples. State selective absorption imaging can deliver spatially resolved information about the spin state, also for samples at μK temperatures. Using these methods, we have determined an upper bound for the ^{87}Sr spin relaxation rate and have found it to be low, as expected. These methods will be necessary tools for the implementation of quantum simulations and quantum computation making use of the ^{87}Sr nuclear spin.

Acknowledgments

We gratefully acknowledge support from the Austrian Ministry of Science and Research (BMWF) and the Austrian Science Fund (FWF) through a START grant under project number Y507-N20 as well as support from the European Commission under project number 250072 iSENSE.

-
- [1] M. A. Cazalilla, A. Ho, and M. Ueda, *New J. Phys.* **11**, 103033 (2009).
 - [2] A. Gorshkov, M. Hermele, V. Gurarie, C. Xu, P. Julienne, J. Ye, P. Zoller, E. Demler, M. D. Lukin, and A. M. Rey, *Nature Phys.* **6**, 289 (2010).
 - [3] C. Wu, J.-P. Hu, and S.-C. Zhang, *Phys. Rev. Lett.* **91**, 186402 (2003).
 - [4] C. Wu, *Mod. Phys. Lett. B* **20**, 1707 (2006).
 - [5] M. Foss-Feig, M. Hermele, and A. M. Rey, *Phys. Rev. A* **81**, 051603 (2010).
 - [6] M. Hermele, V. Gurarie, and A. M. Rey, *Phys. Rev. Lett.* **103**, 135301 (2009).
 - [7] C. Xu, *Phys. Rev. B* **81**, 144431 (2010).
 - [8] H.-H. Hung, Y. Wang, and C. Wu, arXiv:1103.1926 (2011).
 - [9] F. Gerbier and J. Dalibard, *New J. Phys.* **12**, 033007 (2010).
 - [10] N. R. Cooper, *Phys. Rev. Lett.* **106**, 175301 (2011).
 - [11] B. Béri and N. R. Cooper, arXiv:1105.1252 (2011).
 - [12] A. Górecka, B. Grémaud, and C. Miniatura, arXiv:1105.3535 (2011).
 - [13] A. J. Daley, M. M. Boyd, J. Ye, and P. Zoller, *Phys. Rev. Lett.* **101**, 170504 (2008).
 - [14] A. V. Gorshkov, A. M. Rey, A. J. Daley, M. M. Boyd, J. Ye, P. Zoller, and M. D. Lukin, *Phys. Rev. Lett.* **102**, 110503 (2009).
 - [15] T. Fukuhara, Y. Takasu, M. Kumakura, and Y. Takahashi, *Phys. Rev. Lett.* **98**, 030401 (2007).
 - [16] S. Taie, Y. Takasu, S. Sugawa, R. Yamazaki, T. Tsujimoto, R. Murakami, and Y. Takahashi, *Phys. Rev. Lett.* **105**, 190401 (2010).
 - [17] B. J. DeSalvo, M. Yan, P. G. Mickelson, Y. N. Martinez de Escobar, and T. C. Killian, *Phys. Rev. Lett.* **105**, 030402 (2010).
 - [18] M. K. Tey, S. Stellmer, R. Grimm, and F. Schreck, *Phys. Rev. A* **82**, 011608(R) (2010).
 - [19] T. Mukaiyama, H. Katori, T. Ido, Y. Li, and M. Kuwata-Gonokami, *Phys. Rev. Lett.* **90**, 113002 (2003).
 - [20] M. M. Boyd, T. Zelevinsky, A. D. Ludlow, S. Blatt, T. Zanon-Willette, S. M. Foreman, and J. Ye, *Phys. Rev. A* **76**, 022510 (2007).
 - [21] W. Gerlach and O. Stern, *Z. Phys.* **8**, 110 (1922).
 - [22] D. M. Stamper-Kurn, M. R. Andrews, A. P. Chikkatur, S. Inouye, H.-J. Miesner, J. Stenger, and W. Ketterle, *Phys. Rev. Lett.* **80**, 2027 (1998).
 - [23] T. Sleator, T. Pfau, V. Balykin, O. Carnal, and J. Mlynek, *Phys. Rev. Lett.* **68**, 1996 (1992).
 - [24] H. J. Metcalf and P. van der Straten, *Laser Cooling and Trapping* (Springer, New York, 1999).
 - [25] Assuming OSG beam intensities different by $\pm 20\%$ from the measured values did not change the outcome of the simulation significantly after fitting OSG beam waists and positions again.
 - [26] M. R. Matthews, D. S. Hall, D. S. Jin, J. R. Ensher, C. E. Wieman, E. A. Cornell, F. Dalfovo, C. Minniti, and S. Stringari, *Phys. Rev. Lett.* **81**, 243 (1998).
 - [27] The simulation determines the average number of photons scattered by an atom in a certain m_F state for a distribution of atoms corresponding to the one used in our experiment. It takes into account the Zeeman splitting of the excited state, the Doppler shift, acceleration of atoms by photon absorption and emission, and optical pumping. The result of the simulation is that the number of photons absorbed by an atom initially in a certain m_F state is to within 10% proportional to the line strength of the transition corresponding to this m_F

state.

[28] P. S. Julienne, private communication.